AIMS Materials Science, 13(5): 967–975.
DOI: 10.3934/matersci.2026045
Received: 29 August 2026
Revised: 12 October 2026
Accepted: 26 October 2026
Published: 30 October 2026

https://www.aimspress.com/journal/Materials

Research article

Nitrogen-doped carbon with three-dimensional interconnected wrinkled lamellar hierarchical porous framework for high-performance aqueous Zn-I_2 batteries

Xianhe Meng[1,2,*], Qi Shen[2], Aobo Yue[2], Tao Chen[3] and Zonghua Wang[1,*]

[1] College of Chemistry and Chemical Engineering, Qingdao University, Qingdao 266071, China
[2] College of Materials and Chemistry, China Jiliang University, Hangzhou 310018, China
[3] Shaoxing Electric Power Equipment Co., Ltd. Shaoxing 312000, China

* **Correspondence:** Email: mengxhe@cjlu.edu.cn, wangzonghua@qdu.edu.cn; Tel: +86-0571-86835740, +86-0532-85951196.

Abstract: Aqueous zinc-iodine (Zn-I_2) batteries are promising for large-scale energy storage, yet their practical deployment is severely restricted by polyiodide shuttle behavior and the poor intrinsic conductivity of iodine active species. In this work, nitrogen-doped carbon (C-Z-K) with a three-dimensional interconnected wrinkled lamellar hierarchical porous framework is synthesized via high-temperature calcination of dual precursors zeolitic imidazolate framework-8 (ZIF-8)-gel and potassium citrate. When utilized as an iodine host for Zn-I_2 batteries, the optimized material achieves an initial specific capacity of 132.9 mAh g^{-1} and maintains 97.3% capacity retention after 800 continuous cycles versus the 50th cycle capacity. The hierarchically micro-mesoporous structure coupled with nitrogen heteroatom doping works synergistically to suppress the harmful polyiodide shuttle effect, reinforce physical-chemical confinement toward iodine species, and accelerate electronic and ionic transport. Electrochemical characterizations confirm favorable charge-transfer kinetics, superior long-term cyclability, and competitive rate performance. This study provides an instructive approach to construct metal-organic framework (MOF)-derived porous carbon hosts for high-performance aqueous Zn-I_2 battery systems.

Keywords: ZIF-8-gel; interconnected wrinkled lamellar framework; porous carbon; N-doping; Zn-I_2 batteries

1. Introduction

Renewable energy integration hinges on advanced energy storage systems. Aqueous zinc-iodine (Zn-I_2) batteries stand out among numerous energy storage devices by virtue of their abundant raw materials, inherent operational safety, favorable reaction kinetics, and a high theoretical energy density of 220 Wh kg^{-1}, showing great application potential for large-scale energy storage [1,2]. Nevertheless, the practical deployment of Zn-I_2 batteries is severely hindered by two key bottlenecks: the low intrinsic electronic conductivity of elemental iodine and the notorious polyiodide shuttle effect arising from the dissolution of intermediate polyiodide ions (I_3^-/I_5^-) in aqueous electrolytes [3–6]. The shuttle effect not only causes active material loss and low Coulombic efficiency but also leads to rapid capacity decay during long-term cycling.

To tackle these issues, constructing porous carbon hosts to immobilize iodine species has become a mainstream research strategy [7–10]. Recent studies have clarified that the confinement of iodine species in carbon hosts is governed by both physical pore architecture and chemical surface functionality; micropores/mesopores and pore connectivity control spatial encapsulation and ion transport, while heteroatoms (e.g., N and O provide polar anchoring sites and can catalyze the I_2/I^- redox conversion [11,12]. This structure-confinement correlation offers a rational principle for designing high-performance iodine hosts. Among various carbon materials, nitrogen-doped carbon derived from metal-organic frameworks (MOFs) has been widely studied on account of its developed pore structure and abundant surface active sites, which can physically adsorb iodine and chemically anchor polyiodides via functional groups [13–16]. Nitrogen-doped MOF-derived carbons, exemplified by zeolitic imidazolate framework-8 (ZIF-8) derivatives, show promise via pore adsorption and surface functionalization [17–19]. The derivative materials of ZIF-8 often contain active elements, such as nitrogen and oxygen, which are beneficial for fixing iodine and improving the performance of Zn-I_2 batteries [20–22]. However, conventional designs suffer from insufficient pore connectivity or inactive sites under high-rate conditions. Herein, we prepared a N-doped porous carbon with a 3D interconnected wrinkled layered hierarchical structure from ZIF-8-gel and potassium citrate by a dual-template method. Unlike conventional iodine hosts that rely on a single activation route and are dominated by micropores with limited pore connectivity [23], this dual-template strategy creates a hierarchical framework with high surface area and continuous mesoporous channels, enabling effective physical confinement and fast ion/electron transport even at high iodine loading. In addition, compared with directly carbonized ZIF-8-derived carbons that retain N-doped sites but often suffer from insufficient mesoporosity and pore connectivity [24,25], the ZIF-8-gel/potassium citrate route simultaneously optimizes the hierarchical pore structure and N-doped chemical anchoring. The electrode delivers 132.9 mAh g^{-1} initial capacity at 1 C and good capacity retention after 800 cycles offering a new design strategy for high-performance Zn-I_2 battery cathode hosts.

2. Materials and methods

The ZIF-8-gel (Figure S1) synthesized according to previous literature [26] and potassium citrate mixture (mass ratio 1:5) was ball-milled in air (ball/material = 20:1, 1 h) and then calcined at 900 °C for 2 h under Ar with a ramp rate of 10 °C/min. The product (C-Z-K) was washed with dilute HCl and deionized water and vacuum-dried at 120 °C for 12 h. C-Z and C-K reference samples were synthesized

with identical parameters directly from ZIF-8-gel and potassium citrate, respectively. Detailed information (reagents, electrochemical method, etc.) is available in Supplementary Information.

3. Results and discussion

Unlike ZIF-8 synthesized by conventional solvent method, which has a regular rhombic dodecahedron shape, ZIF-8-gel exhibits spherical nanoparticle accumulation (Figure S2). X-ray diffraction (XRD) patterns (Figure 1a) were used to analyze the crystal structure of the prepared. The XRD patterns revealed that ZIF-8-gel exhibited diffraction peak signals at 6.5°, 10.3°, 12.8°, 18.1°, and 26.7°, which corresponded to the typical main peak positions of simulated crystalline ZIF-8 indicating the successful preparation of ZIF-8-gel [26,27]. The broader peaks suggested smaller grain sizes and the presence of nanocrystals. Moreover, scanning electron microscopy (SEM) showed that the morphology of ZIF-8-gel was the accumulation of nanoparticles (Figure S2). After carbonization, the XRD pattern of C-Z-K (Figure 1b) exhibits two broad diffraction peaks. The prominent peak centered at approximately 22° corresponds to the (002) plane of amorphous/disordered graphitic carbon. Additionally, a relatively broad and weak diffraction peak located at around 43° can be indexed to the (100) in-plane crystal plane of carbon materials. The coexistence of the broad (002) and (100) reflections indicates that C-Z-K possesses a predominantly amorphous framework with a certain degree of local short-range graphitic ordering, which is beneficial for enhancing electronic conductivity while maintaining a high-surface-area porous structure.

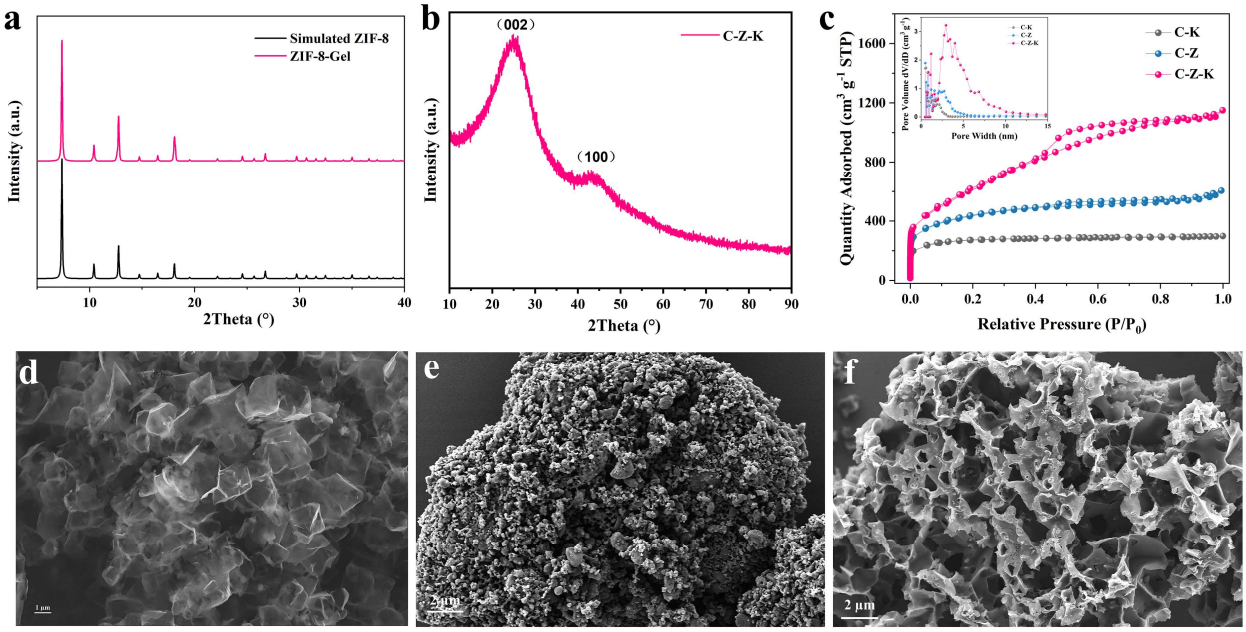


Figure 1. (a) XRD patterns of simulated ZIF-8, ZIF-8-gel. (b) The XRD pattern of C-Z-K. (c) Isothermal adsorption curves of C-K, C-Z and C-Z-K (insert curve is the pore size distribution). (d–f) The SEM images of C-K, C-Z and C-Z-K, respectively.

In order to explore the pore structure, nitrogen adsorption-desorption isothermal tests were carried out on three carbon materials (Figure 1c). The brunauer-emmett-teller (BET) surface areas of C-Z, C-K, and C-Z-K are 988.2, 1518.8, and 2168.4 m^2 g^{-1}, and the Langmuir surface areas of C-Z, C-K,

and C-Z-K are 1230.2, 2126.4, and 3531.8 m^2 g^{-1}, respectively. Combined with the pore size distribution diagram, it can be found that the prepared carbon materials not only have micropores but also have a certain amount of mesoporous structure. Moreover, the pore size of C-K and C-Z is concentrated in the micropore area, while the pore size distribution center of C-Z-K is about 3 nm and has a wider mesoporous region (2–12 nm). Consistent with the pore analysis, C-Z-K possesses the richest pore structure and highest specific surface area. SEM images (Figure 1d–f) reveal that C-K exhibits a stacked sheet morphology, C-Z consists of stacked small nanoparticles, and C-Z-K displays a three-dimensional interconnected wrinkled lamellar hierarchical porous framework. The energy-dispersive X-ray spectroscopy (EDS) point scanning (Figure S3) further confirms the presence of heteroatoms N and O in C-Z-K, with contents of 0.96 wt.% and 10.10 wt.%, respectively. To further evaluate the surface chemistry, high-resolution X-ray photoelectron spectroscopy (XPS) measurements were conducted. As shown in Figure S4a, the XPS survey spectrum confirms the coexistence of C, N, and O in the C-Z-K sample. In the C 1s spectrum (Figure S4b), four subpeaks obtained by peak fitting demonstrate the successful incorporation of N and O heteroatoms into the carbon framework. The N 1s spectrum (Figure S4c) reveals that the nitrogen species are predominantly active pyridinic-N and pyrrolic-N, which provide strong Lewis base sites to chemically anchor polyiodides. Combined with the abundant oxygen-containing functional groups (Figure S4d) and the 3D hierarchical porous framework, these active sites synergistically enhance iodine confinement and electrochemical kinetics.

Figure 2a shows two broad Raman peaks approximately at 1340 and 1580 cm^{-1} of the three carbon materials, which can be assigned to the D and G bands of disordered and graphitized carbons, respectively. Through curve Gaussian fitting (Figure S5), the ID/IG of C-Z-K, C-Z and C-K are 1.42, 1.48 and 1.54, respectively, indicating that the graphitization degree of the materials is not different with a certain amount of defects [28]. The higher degree of graphitization of C-Z-K indicates that it has better electron conductivity. Porous carbon materials are very effective for the application of iodine storage in Zn-I_2 batteries. By adding three kinds of carbon materials loaded with iodine to 2M $ZnSO_4$ solution and standing for 96 h, the results shown in Figure 2b are obtained. There is almost no I_2 precipitation from the perspective of color change, indicating that the iodine fixation ability of C-Z-K is significantly stronger than that of the other two carbon materials. Moreover, the elemental mapping (EDS) of C, N, and I in Figure 2c showed a uniform distribution in the I_2@C-Z-K composites.

Cyclic voltammetry (CV) measurements were performed to probe electrochemical behaviors of three cathode-based batteries. CV scans (0.6–1.6 V, 1 mV s^{-1}, Figure S6a) for I_2@C-Z-K, I_2@C-Z, and I_2@C-K all feature symmetric single redox peaks, consistent with a reversible $I_2 \leftrightarrow 2I^-$ conversion as the dominant redox process, although trace or short-lived polyiodide intermediates cannot be completely excluded under these conditions. This dominant pathway improves iodine conversion kinetics and lowers energy loss. I_2@C-Z has a small peak separation of 0.11 V, signifying weak polarization and rapid kinetics. I_2@C-Z-K shows no obvious peak shift in 1.1–1.4 V for three initial cycles (Figure S6b), confirming superior reversibility and cycling stability. Even at different scanning rates, there was always and only one pair of redox peaks (Figure 2d). As the scan rate increases from 0.5 to 5 mV s^{-1}, both the peak current and peak potential difference increase. Figure 2e presents the power-law relationship between scan rate and peak current ($i = av^b$), where $b = 0.5$ signifies diffusion-controlled kinetics and $b = 1.0$ indicates capacitive behavior [8]. Linear fitting yields b values of 0.73 (cathodic) and 0.71 (anodic) for the I_2@C-Z-K electrode, implying a hybrid mechanism combining battery-type and capacitive contributions. Figure S7 quantitatively compares the capacitive contribution ratios of I_2@C-Z-K at scan rates ranging from 0.5 to 5.0 mV s^{-1}. With increasing scan

rate, the value gradually increased from 61.51% to 92.19%. This capacitive behavior highlights the excellent kinetic performance of I_2@C-Z-K, in which the hierarchical porous structure and nitrogen doping not only synergistically enhance the surface-controlled charge storage mechanism but also preserve the integrity of the active material, thereby facilitating highly reversible redox reactions. Separately, a Zn-I_2 test-tube battery was assembled, and reaction intermediates were probed via in situ ultraviolet-visible (UV-vis) spectroscopy. During test-tube battery operation, the electrolyte remained clear with no yellow I_3^- coloration (Figure 2f). UV–vis spectra initially showed only the 198 nm peak of 2 M $ZnSO_4$ (Figure 2g); upon cycling, the 215 nm ZnI_2 band intensified [9]. Discharge ($I_2 + 2e^- \rightarrow 2I^-$) produces I^- that dissolves in the excess electrolyte; however, no obvious I_3^- signal at 288 nm was observed throughout the measurements, indicating that any polyiodide intermediates formed did not accumulate to a spectroscopically detectable level under the present conditions. This is consistent with the visual observation. The micro/mesoporous N-doped carbon confines iodine species and the reduction reaction, suppresses I_3^- dissolution/shuttling, and thus improves performance. These results suggest that the iodine redox process is dominated by I_2/I^- conversion, while the presence of small amounts of short-lived or low-concentration polyiodide intermediates cannot be fully ruled out.

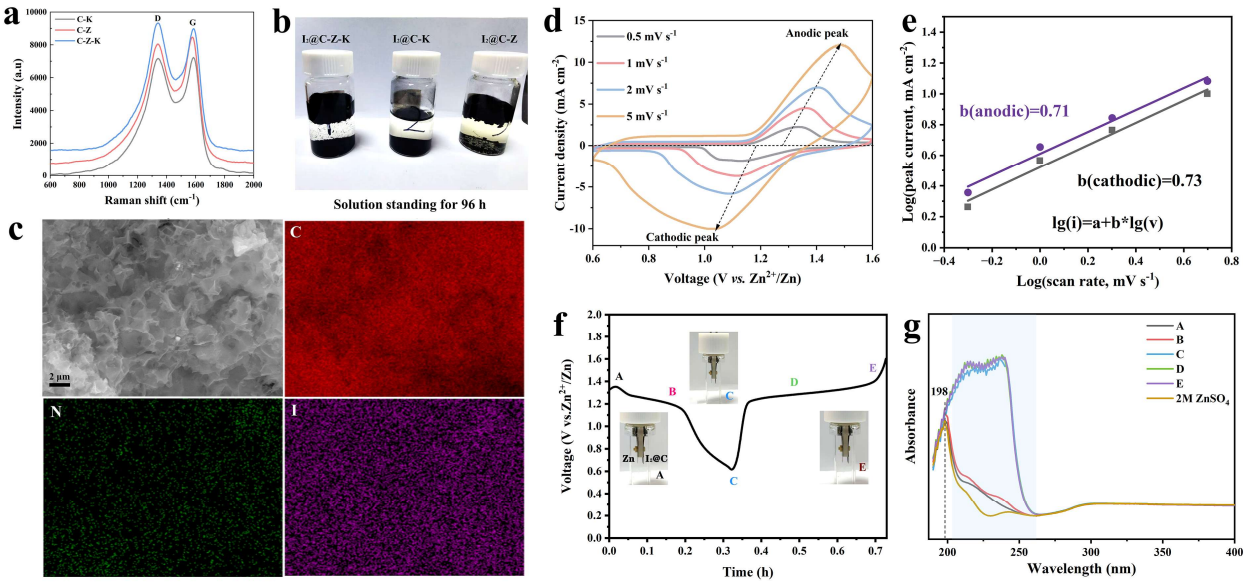


Figure 2. (a) The Raman spectra of C-K, C-Z and C-Z-K. (b) Photos of I_2@C after standing in 2M $ZnSO_4$ for 96 h. (c) The SEM and EDS images of I_2@C-Z-K. (d) CV curves of I_2@C-Z-K at different sweep speeds. (e) Dependence of the anodic and cathodic peak currents on the scan rate. (f) Different states in the first cycle for in-situ UV-vis at 1 C charge discharge rate. (g) In-situ UV-vis spectra of Zn-I_2 cuvette battery.

To further verify the electrochemical stability of the I_2@C-Z-K electrode material, the long-cycle performance of the battery was tested at different charge-discharge rates. As shown in Figure 3a, the initial capacities of I_2@C-Z-K, I_2@C-Z, and I_2@C-K at 1C were 132.9, 101.6, and 67.0 mAh g^{-1}, respectively. And, the Coulomb efficiency of three electrodes remained stable at 100%, indicating that the material had excellent reversibility and a potentially long service life. It should be noted that these specific capacities were evaluated based on the total mass of the I_2@C composite cathode material. Figure 3b shows the rate performance curve of I_2@C-Z-K tested at current rates from 1 C to 10 C.

When the current returned to 1 C, the specific capacity recovered to 89.7 mAh g^{-1} indicating that the I_2@C-Z-K electrode had good rate performance and cycle stability. Electrochemical impedance spectroscopy (EIS) was employed to compare the electrode performance by analyzing the high-frequency contact resistance (Rs), which reflects the internal contact impedance of the cell [17,28]. The initial Rs values of I_2@C-Z-K, I_2@C-Z, and I_2@C-K cathodes were 1.81, 3.99, and 9.11 Ω (Figure S8), and increased to 4.32, 8.50, and 13.13 Ω after 10 cycles (Figure 3c). A lower Rs can reduce the internal resistance and interfacial contact resistance of the cell, improve electron/ion transport and current distribution, and thereby indirectly facilitate the insertion/extraction of iodide ions, thus enhancing battery efficiency, power density, structural stability, and cycling life. Figure 3d shows the Zn/C-Z-K@I_2 battery and its charge-discharge principle. Then, when cycled at 2C for 800 cycles (Figure 3e), the I_2@C-Z-K, I_2@C-Z and I_2@C-K electrodes deliver specific capacities of 98.2, 68.2 and 69.3 mAh g^{-1}, with capacity retentions of 97.3%, 90.7%, and 100.8% versus their 50th cycle capacities and 76.4%, 66.4%, and 97.1% versus their initial capacities. The I_2@C-K with regular sheet carbon structure shows the best long cycle stability but the capacity is low, while the I_2@C-Z-K with 3D interconnected structure and N-doping shows the best specific capacity and good long cycle stability.

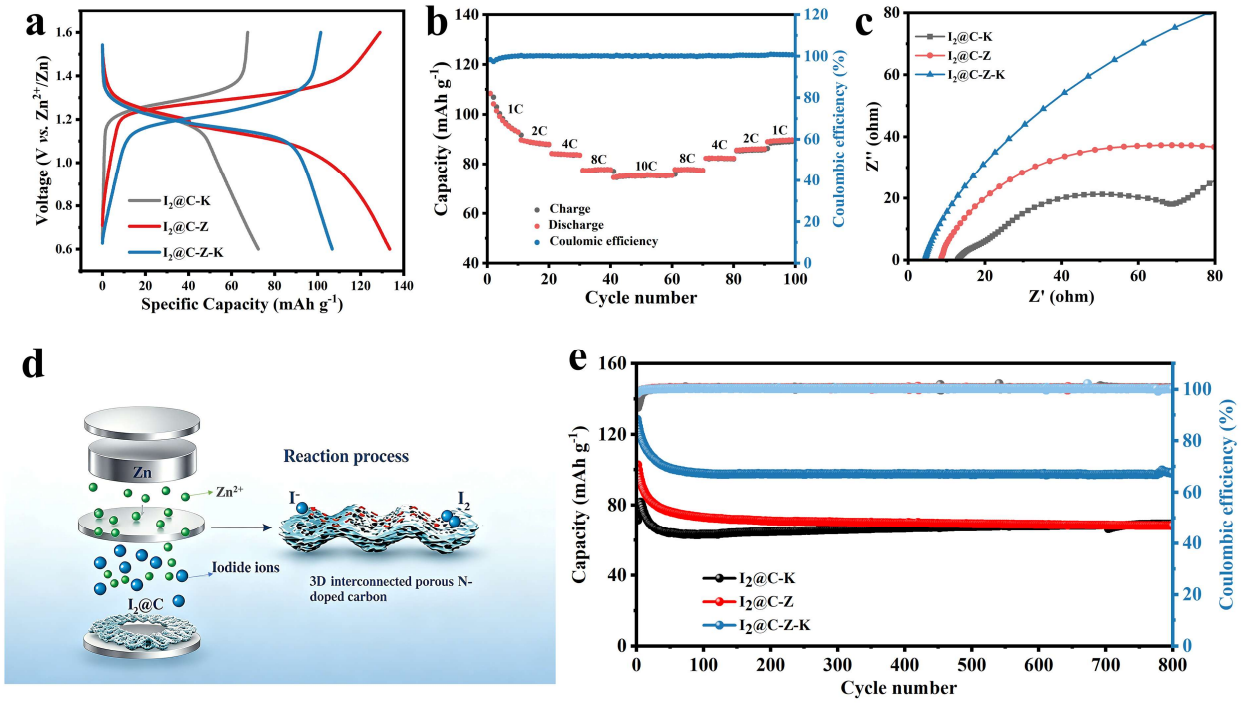


Figure 3. (a) The initial charge-discharge curve of electrode materials at 1 C. (b) Rate performance under different rate charge discharge current of Zn-I_2 battery with I_2@C-Z-K. (c) The Nyquist plots of Zn/C-I_2 batteries after 10 cycles. (d) Schematic illustration of Zn/C-I_2 battery. (e) Prolonged cyclic performance of Zn/C-I_2 batteries at 2 C.

4. Conclusions

In summary, the dual-template method yielded porous N-doped carbon C-Z-K with interconnected wrinkled lamellar hierarchical structure and nitrogen active sites. The synergism of its 3D conductive network restrains the polyiodide shuttle effect and accelerates charge transport. Electrochemical characterizations confirm its high capacity, good cycling stability, and rate capability, laying a

foundation for optimizing MOF-based carbon materials for aqueous Zn-I_2 batteries. Follow-up studies will focus on optimizing pore engineering and exploring hybrid composites to boost practical performance.

Use of AI tools declaration

The authors declare they have not used Artificial Intelligence (AI) tools in the creation of this article.

Acknowledgments

This work was supported by the Funds of the Natural Science Foundation of Hangzhou (2025SZRJJ2021), the Central Guidance on Local Science and Technology Development Fund of Sichuan Province (202502ZYDF031).

Author contributions

Xianhe Meng: investigation, writing–original draft, funding acquisition, conceptualization, writing–review & editing; Qi Shen: data curation, investigation, methodology; Aobo Yue: visualization, formal analysis, validation; Tao Chen: supervision, resources; Zonghua Wang: writing–review & editing, supervision, project administration, conceptualization.

Conflict of interest

The authors declare no conflict of interest.

References

1. Ran Y, Dong F, Sun S, et al. (2026) Aqueous zinc-based batteries: Active materials, device design, and future perspectives. *Adv Energy Mater* 16: 2406139. https://doi.org/10.1002/aenm.202406139
2. Huang F, Xu W, He Y, et al. (2025) Electrolyte design toward high-performance zinc-iodine batteries: Progress, challenges, and prospects. *Battery Energy* 4: e70036. https://doi.org/10.1002/bte2.20250017
3. Qi D, Jiang H, Chen X, et al. (2025) Design strategies, challenges, and prospects of nanomaterials for aqueous Zn-iodine batteries. *ACS Nano* 19: 24592–24620. https://doi.org/10.1021/acsnano.5c06585
4. Wang L, Ji P, Li N, et al. (2025) Advancements and challenges in aqueous zinc-iodine batteries: Strategies for enhanced performance and stability. *Electrochem Energy Rev* 8: 34. https://doi.org/10.1007/s41918-025-00274-9
5. Bai Z, Wang G, Liu H, et al. (2024) Advancements in aqueous zinc-iodine batteries: A review. *Chem Sci* 15: 3071–3092. https://doi.org/10.1039/d3sc06150g
6. Chen S, Zeng S, Ao Z, et al. (2025) α-Trehalose: A multifunctional electrolyte additive for advanced aqueous Zn-I_2 batteries under high Zn depth of discharge. *Electr Act* 514: 145515. https://doi.org/10.1016/j.electacta.2024.145515

7. Qian Y, Chang G, Huang C, et al. (2025) Three-pronged approach enhances porous carbon spheres for high-performance aqueous zinc-iodine batteries. *ACS SCE* 13: 12057–12066. https://doi.org/10.1021/acssuschemeng.5c03672.s001
8. Wu Y, Qian Y, Huang C, et al. (2023) Hierarchical porous soft carbon host for the cathode of an aqueous zinc-iodine battery with ultra-long cycle life. *Electr Act* 460: 142593. https://doi.org/10.1016/j.electacta.2023.142593
9. Yan L, Liu T, Zeng X, et al. (2022) Multifunctional porous carbon strategy assisting high-performance aqueous zinc-iodine battery. *Carbon* 187: 145–152. https://doi.org/10.1016/j.carbon.2021.11.007
10. Zeng S, Chen S, Ao Z, et al. (2025) Dual-mechanism anchoring of iodine species by pitch-derived porous carbon for enhanced zinc-iodine battery performance. *Small* 21: 2501695. https://doi.org/10.1002/smll.202501695
11. Guo H, Luo H, Zhu F, et al. (2026) Mechanical-thermal decoupling engineering unlocks ultra-stable dry thick iodine cathodes for Ah-level zinc-based pouch batteries. *Adv Mater* 38: e73037. https://doi.org/10.1002/adma.73037
12. Su X, Li S, Chen Z, et al. (2026) Steering $Zn(ClO_4)_2$ electrolyte: Trifunctional polycationic artificial interphase for wide-temperature Ah-level Zn-I_2 pouch cells. *Energy Storage Mater* 85: 104900. https://doi.org/10.1016/j.ensm.2026.104900
13. Mourdikoudis S, Dutta S, Kamal S, et al. (2025) State-of-the-art, insights, and perspectives for MOFs-nanocomposites and MOF-derived (nano)materials. *Adv Mater* 37: 2415399. https://doi.org/10.1002/adma.202415399
14. Liu Y, Wu X, Bando Y (2025) Toward highly durable aqueous zinc ion batteries: A review of MOFs/MOF-derived cathode materials. *Inorg Chem Front* 12: 3959–3980. https://doi.org/10.1039/D5QI00555H
15. Mohtaram MS, Abolghasemi A, Sayahi S, et al. (2026) MOF-derived nanomaterials: Transformative innovations for renewable energy and environmental sustainability. *Coordin Chem Rev* 546: 217083. https://doi.org/10.1016/j.ccr.2025.217083
16. Chai L, Li R, Sun Y, et al. (2025) MOF-derived carbon-based materials for energy-related applications. *Adv Mater* 37: 2413658. https://doi.org/10.1002/adma.202413658
17. Liu Q, Wang S, Lang J, et al. (2025) Atomic synergy catalysis enables high-performing aqueous zinc-iodine batteries. *Nano Lett* 25: 6661–6669. https://doi.org/10.1021/acs.nanolett.5c00279
18. Miensah ED, Chen J, Gu A, et al. (2021) Ultrahigh capture of radioiodine with zinc oxide-decorated, nitrogen-doped hierarchical nanoporous carbon derived from sonicated ZIF-8-precursor. *J Mater Sci* 56: 9106–9121. https://doi.org/10.1007/s10853-021-05887-1
19. Yang Q, Qiao Y, Tong R, et al. (2026) Multi-site co-doped hierarchical porous carbon for efficient Iodine conversion and uniform zinc deposition in zinc-iodine batteries. *Small Methods* 10: e02240. https://doi.org/10.1002/smtd.202502240
20. Tang L, Gao J, Shen T, et al. (2025) N, O co-doped porous carbon host with interconnected reaction microenvironments for long-life zinc-iodine batteries. *Chem Eng J* 517: 164383. https://doi.org/10.1016/j.cej.2025.164383
21. Zheng R, Guo Y, Hu J, et al. (2026) N-doped hierarchical porous carbon nanofibers as efficient hosts for stabling iodine redox kinetics. *J Energy Storage* 152: 120520. https://doi.org/10.1016/j.est.2026.120520

22. Xu X, Huo R, Tang Z, et al. (2026) Synergistic anion-mediated conversion and single-atom catalysis enable fast and reversible iodine redox kinetics. *ACS Electrochem* 2: 1572–1582. https://doi.org/10.1021/acselectrochem.6c00132
23. Sun J, Ma H, Wang D (2023) Heavily heteroatoms doped carbons with tunable microstructure as the iodine hosts for rechargeable zinc-iodine aqueous batteries. *J Alloys Compd* 947: 169696. https://doi.org/10.1016/j.jallcom.2023.169696
24. Sun J, Wang Z, Zhang J, et al. (2024) Shuttle-free zinc-iodine batteries enabled by a cobalt single atom anchored on N-doped porous carbon host with ultra-high specific surface area. *J Energy Storage* 90: 111716. https://doi.org/10.1016/j.est.2024.111716
25. Wang D, Kong X, Wang Z, et al. (2025) Dual-functional Fe_3O_4-decorated porous carbon nanosheets for kinetics-enhanced aqueous zinc-iodine batteries. *Green Carbon* 3: 382–392. https://doi.org/10.1016/j.greenca.2025.06.005
26. Chaudhari A, Tan J (2017) A mechano-responsive supramolecular metal-organic framework (supraMOF) gel material rich in ZIF-8 nanoplates. *Chem Commun* 53: 8502–8505. https://doi.org/10.1039/c7cc03478d
27. Feng X, Liu C, Ren K, et al. (2025) In-situ synthesis of ZIF-8 gel network in mixed matrix membranes for enhanced CO_2/N_2 separations. *Chem Eng Sci* 311: 121610. https://doi.org/10.1016/j.ces.2025.121610
28. He Y, Liu M, Chen S, et al. (2022) Shapeable carbon fiber networks with hierarchical porous structure for high-performance Zn-I_2 batteries. *Sci China Chem* 65: 391–398. https://doi.org/10.1007/s11426-021-1177-1



AIMS Press

© 2026 the Author(s), licensee AIMS Press. This is an open access article distributed under the terms of the Creative Commons Attribution License (https://creativecommons.org/licenses/by/4.0)